

Superconductivity in Epitaxial SiGe for Cryogenic Electronics

Julian A. Steele^{1,2,*}, Patrick J. Strohbeen^{3,*}, Carla Verdi¹, Ardeshir Baktash^{2,4},
Alisa Danilenko³, Yi-Hsun Chen¹, Jechiel van Dijk³, Lianzhou Wang^{2,4}, Eugene
Demler⁵, Salva Salmani-Rezaie⁶, Peter Jacobson^{1,7,†} and Javad Shabani^{3‡}

¹ *School of Mathematics and Physics, The University of Queensland, Brisbane, QLD 4072, Australia*

² *Australian Institute for Bioengineering and Nanotechnology,
The University of Queensland, St Lucia, QLD 4072, Australia*

³ *Center for Quantum Information Physics, New York University, New York, NY 10003, USA*

⁴ *School of Chemical Engineering, The University of Queensland, St Lucia, QLD 4072, Australia*

⁵ *Institute for Theoretical Physics, ETH Zürich, Zürich 8093, Switzerland*

⁶ *Department of Materials Science and Engineering,
The Ohio State University, Columbus, OH 43210, USA*

⁷ *ARC Centre of Excellence for Engineered Quantum Systems, Brisbane, QLD 4072, Australia*

Introducing superconductivity into group IV elements by doping has long promised a pathway to introduce quantum functionalities into well-established semiconductor technologies. The non-equilibrium hyperdoping of group III atoms into Si or Ge has successfully shown superconductivity can be achieved, however, the origin of superconductivity has been obscured by structural disorder and dopant clustering. Here, we report the epitaxial growth of hyperdoped Ga:Ge films by molecular beam epitaxy with extreme hole concentrations ($n_h = 4.15 \times 10^{21} \text{ cm}^{-3}$, 17.9% Ga substitution) that yield superconductivity with a critical temperature of $T_C = 3.5 \text{ K}$, and an out-of-plane critical field of 1 T at 270 mK. Synchrotron-based X-ray absorption and scattering methods reveal that Ga dopants are substitutionally incorporated within the Ge lattice, introducing a tetragonal distortion to the crystal unit cell. Our findings, corroborated by first-principles calculations, suggest that the structural order of Ga dopants creates a flat band for the emergence of superconductivity in Ge, establishing hyperdoped Ga:Ge as a low-disorder, epitaxial superconductor-semiconductor platform.

I. INTRODUCTION

Integrating superconductors with semiconductor heterostructures is emerging as a central theme across quantum technologies. By combining these distinct material classes, devices can leverage macroscopic superconducting coherence with semiconductor microscopic degrees of freedom to enable technologies such as magnetic field sensors, single-photon detectors, low noise amplifiers, and new potential avenues for realization of topological superconductivity [1–3] and the development of gate-tunable transmon (gatemon) qubits [4–8].

Germanium has emerged as a critical semiconductor for quantum devices due to its compatibility with silicon foundry processes (including SiGe alloying), record high hole mobilities [9], and strong spin-orbit coupling [10]. Given the maturity and versatility of Ge, recent work has focused on quantum coherent phenomena in the context of circuit quantum electrodynamics [10, 11], and Ge remains at the forefront of searches for topological electronic states [12]. For Ge-based quantum devices, traditional superconductors (Al, Nb, NbTiN) and newer candidates (PtSiGe, TaGe) [12, 13] are promising due to their compatibility with Ge and SiGe material platforms and processes. However, interfacial and bulk disorder

remains a concern for superconductor-semiconductor devices as it is known to limit device performance and is believed to suppress topological superconductivity [14].

In recent years, there has been great progress in developing single epitaxial interfaces between superconductors and III/V semiconductors (S-Sm) [1, 15]. Yet, a critical challenge remains in creating superconductor-semiconductor-superconductor (S-Sm-S) hybrid platforms due to surface energy mismatch during thin film epitaxy leading to three-dimensional growth [16], chemical intermixing at metal-semiconductor interfaces [16, 17], and the need for coherent interfaces rather than amorphous stacks [18]. Minimizing material disorder is critical for avoiding quasiparticle poisoning [19–21], decreasing two-level system centers for qubits [22], ensuring reproducible transport characteristics in (epitaxial vertical) Josephson junctions [18], and exploring exotic quantum phases of matter [14, 23]. One promising way forward is to sidestep disordered interfaces between dissimilar materials and induce superconductivity within a semiconducting host that can be grown via thin film epitaxy [24].

In covalent semiconductors such as diamond, heavy doping (e.g. with boron) can lead to superconductivity [25]. A similar approach has been extended to Ge using extremely high p-type doping levels, far exceeding what is typical for standard semiconductor devices [26–28]. These high doping levels, above the miscibility limit of Ga in crystalline Ge (1.8 at.% at 300 K [29]), are

* These authors contributed equally.

† p.jacobson@uq.edu.au

‡ jshabani@nyu.edu

typically introduced by high-energy techniques such as ion implantation and flash annealing. While these doping strategies lead to superconductivity [26–28], key open questions include the presence and role of Ga clusters, dopant site preference in the presence of disorder, and the role of superconducting weak links. Nevertheless, materials like hyperdoped Ga:Ge are an attractive option because they could enable fully epitaxial superconductor-semiconductor heterostructures from the same host material, in contrast to traditional material platforms like Al-InAs.

Here, we report on the molecular beam epitaxy (MBE) growth, superconducting properties, and structure of hyperdoped Ga:Ge. Film growth takes place near room temperature ($\sim 60\text{--}100^\circ\text{C}$) and leverages the surfactant behavior of Ga to enhance surface adatom mobility, enabling the preservation of smooth surfaces and single-crystallinity. This behavior is observed during monitoring with reflection high-energy electron diffraction (RHEED) and more details are presented in the Supplemental dataset, Figure S5. For films with an expected Ga doping concentration of 17.9%, we observe a superconducting transition at 3.5 K and a carrier concentration of 4.15×10^{21} holes cm^{-3} (corresponding to 51% doping efficiency). Employing a suite of short- and long-range structural characterization techniques, we demonstrate that Ga substitution is energetically favored within the Ge host lattice, slightly expanding its unit cell such that it becomes tetragonally distorted via epitaxial clamping, similar to the β -Sn phase (tetragonal diamond-type structure). Density functional theory (DFT) calculations of hyperdoped Ga:Ge show a substantial Fermi level shift into the valence band and the flattening of electronic bands at the R point in the Brillouin zone. Our findings establish that superconductivity arises intrinsically from substitutional Ga-doping and flat band physics rather than Ga-cluster-mediated superconducting weak links.

Figure 1a presents a summary of ion implantation and MBE work on superconducting Ge thin films presenting the superconducting transition temperature, T_C , as a function of hole carriers as measured from Hall measurements, n_{Hall} . MBE samples of this work are shown as solid circles. We observe T_C values varying from 0.6 K to 3.5 K across the range of carrier concentrations of $1\text{--}9 \times 10^{21}$ cm^{-3} , with no superconductivity observed below 1×10^{21} cm^{-3} . Compared to previous reports on MBE-grown samples [30], these samples exhibit larger carrier concentrations that are more comparable to ion implantation strategies [26–28], albeit with a slight reduction in superconducting T_C . We note a rough trend in T_C as a function of hole carriers where superconductivity appears near 1×10^{21} cm^{-3} , reaching a maximum near $4\text{--}5 \times 10^{21}$ cm^{-3} that is consistent with the idea that increasing the density of states at the Fermi level increases the superconducting T_C . Figure 1b presents the sheet resistance as a function of temperature for the sample circled in red in Figure

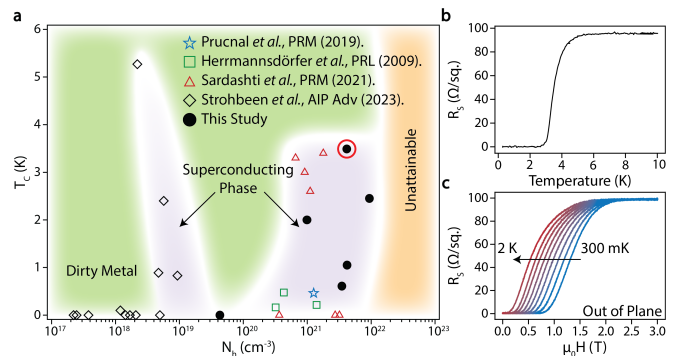


FIG. 1. **a**, Compilation of literature reported superconducting T_C as a function of Hall carriers. The colored star, square, and triangular points were prepared via ion implantation [26–28] while the black diamond [30] and black circles (this study) are MBE-grown samples. The point circled in red is the sample for which sheet resistance during cooldown (**b**) and out of plane H_C (**c**) is presented. The waterfall in **c** is prepared as function of temperature, with the initial trace at the system base temperature of 300 mK up to 2 K.

1a with a T_C of 3.5 K. The critical magnetic field of this sample for an out-of-plane field configuration is also presented in Figure 1c. We observe at 300 mK the out-of-plane H_C to be roughly 1 T, decreasing to 0.14 T at 2 K. In-plane H_C is found to be 3 T, as shown in Figure S6. This value of H_C is significantly enhanced compared to the previous MBE-grown samples [30], and the in-plane critical field behavior is highly favorable for field-dependent applications.

II. RESULTS

A. Dopant fine structure and band structure

To examine the role of Ga as a dopant, we first study the thermodynamic preference and site-specific effects of introducing Ga into the diamond-type Ge crystal using first-principles calculations based on density functional theory (DFT), as detailed in the Methods section. Approximating from our Hall measurements and MBE growth conditions, doping concentrations of 12.5% and 11.1% are simulated for the case of substitutional and interstitial doping, respectively. Figure 2a shows the DFT-optimized structures. Incorporating group-III Ga as a heterovalent dopant within Ge implies some degree of non-equilibrium growth (i.e., the MBE growth process). Subsequently, this results in positive defect formation energy values for cells containing Ga located at both doping sites (Figure 2a and Table S1). However, the formation energy of the substitutional Ga-doped structure (0.314 eV) is markedly lower than a Ge crystal housing Ga at interstitial positions (1.946 eV), indicating that substitutional dopants are expected to be more

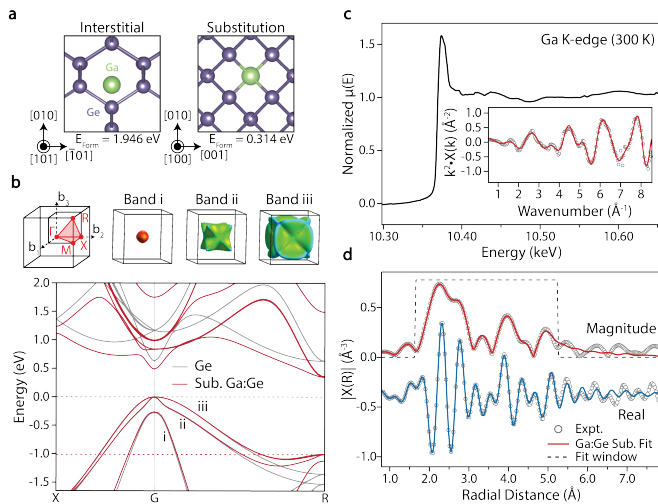


FIG. 2. **a**, Optimized DFT structures of Ga-doped Ge at the interstitial and substitutional sites, along with the defect formation energies (E_{Form}). **b**, Calculated bandstructure along $X-\Gamma$ and $\Gamma-R$ paths in the Brillouin Zone for the diamond cubic germanium crystal. The red lines represent the electronic structure for the substitutionally doped GaGe₇ structure. We present as well the Brillouin Zone with high symmetry points and paths labeled for completeness. The constant energy surfaces for bands i, ii, and iii are presented as well. The predicted flat-band condition is observed as small pockets of high-mass carriers in the surface of Band iii at the corners of the Brillouin Zone. **c**, Experimental Ga-K-edge spectrum (normalized) recorded from the Ga:Ge in fluorescence mode, with its corresponding k^2 -weighted $\chi(k)$ EXAFS data (gray markers) and fit (red line) contained in the inset. **d**, The Fourier-transform magnitude and real part (k^2 -weighted) of the EXAFS data (distances have been phase-corrected). An agreeable fit has been made to the experimental EXAFS using the substitutional doped crystallographic information file (CIF) generated from the optimized DFT calculated structure shown in **a**.

energetically favorable in the material. This is inherently connected to the requirement of the Ge host matrix to undergo an expansion to accommodate the larger Ga atom at the interstitial site, as reported in Table S1. Due to substrate clamping, only the out-of-plane lattice parameter is allowed to relax, resulting in a tetragonal distortion of the cubic unit cell. From our DFT calculations, substituting Ge with Ga at these doping levels is also expected to impart a relatively small out-of-plane expansion of the lattice parameter of 0.12%, resulting in a tetragonal structure (Table S1) to accommodate the heterovalent group-III dopant.

To verify our thermodynamic calculations of the Ga site preference in hyperdoped Ge, we conduct synchrotron X-ray absorption spectroscopy measurements. From our calculations (Figure S9), X-ray absorption of the Ga K-edge is inherently sensitive to the Ga-related local fine structure and can be used to resolve its location within the crystal unambiguously. Experimentally,

we employ extended X-ray absorption fine structure (EXAFS) analysis (using the Ga K-edge), as measured from the Ga:Ge thin film in a fluorescent mode. Multiple spectra were recorded from several locations across the sample, with their average normalized spectra forming the X-ray absorption spectrum shown in Figure 2c. The k^2 -weighted EXAFS signal is shown in the inset, with the corresponding analysis of the Fourier transform presented in Figure 2d. Considering the different structural environments that Ga can occupy in the host Ge crystal (Figure 2a), the EXAFS data are best described by a substitutional doping model with a strong Ge-Ga nearest-neighbor scattering pair at 2.447 \AA , which is close to the calculated length of 2.439 \AA (Figure 2a). To negate other possible coordination environments, such as a-Ga segregation and the interstitial lattice position, Figure S10 further contains the simulated profiles of these potential fine-structure environments using the known crystal structure [31] of α -Ga and our DFT optimized interstitially doped cell. Together, with no strong fine structure observed between 2.5 and 3.8 \AA in the experimental Fourier transform data, these findings confirm that the Ga dopants preferentially occupy substitutional lattice positions, in agreement with our ab initio calculations described above. Furthermore, the relatively large Debye-Waller factors ($\sigma^2(\text{\AA}^2)$) derived from the EXAFS fits (Table S5) highlight the role of both lattice strain and Si diffusion in the Ga:Ge layers.

With confirmation of the substitutional dopant structure via EXAFS, we use the optimized structures shown in Figure 2a to further study how the density of states (DoS) is perturbed through relatively large incorporations of heterovalent Ga dopants at the different lattice sites by calculating the k -resolved bandstructure and k -integrated DoS. The bandstructure calculated for this structure is presented in Figure 2b and the integrated DoS in Figure S8a. From our formation energy calculations, Ga dopants are energetically unlikely to reside at interstitial lattice positions. This is confirmed in the DoS calculation for this system, shown in Figure S8a, which shows that this system is undesirable for preserving the “clean” electronic bands in the host Ge semiconductor. This is evidenced by the disappearance of the parent Ge band gap and the appearance of an electronic instability from localized states due in part to the reduced symmetry of the crystal. In contrast, substitutional Ga doping of the Ge crystal is expected to form acceptor states below the valence band edge of the semiconductor, while the overall band structure near the band gap remains largely unperturbed. This is confirmed by our calculations of the DoS shown in Figure S8a and of the band structure in Figure 2b. An evaluation of the DoS projected onto different atomic orbitals shows that the new, localized states emerge through the hybridization of both the Ga and Ge p-orbitals. As expected, substituting Ge for group III Ga induces p-type doping in the system, with the Fermi level shifting 1.01 eV into the valence band. Furthermore, due

to the lifting of the bands at R , we predict this system to be a candidate flat-band superconductor. By plotting the constant-energy surfaces for the three low-energy bands (band i, ii, and iii), we observe in the surface for band iii, hole pockets of high-mass carriers that cross the Fermi level at the corners of the Brillouin Zone.

B. Epitaxial interfaces and Phonons

Figure 3a presents a schematic structure of the grown film structure with $T_C = 3.5$ K as shown in Figure 1b, in which two hyperdoped Ge layers are grown sandwiching a thin Si buffer layer. Cross-sectional transmission electron microscopy (TEM) and energy dispersive spectroscopy (EDS) measurements are presented in Figure 3b-c and show the spatially homogeneous elemental profile of the Ga dopants throughout the hyperdoped layer. Notably, no distinct signatures of Ga clustering are observed compared to earlier reports where annealing was utilized to activate Ga dopant carriers [28]. Likewise, these MBE-grown materials also exhibit abrupt interfaces and a smooth top surface that is amenable to future planar device fabrication as opposed to previous MBE studies [30]. A view of the atomic structure using low-magnification high-angle annular dark field scanning transmission electron microscopy (HAADF-STEM) is presented in Figure 3d, with a corresponding expansion of the key film/substrate and Ga:Ge/Si interfaces contained in Figure 3e. Owing to the small amount of mismatch strain and thin layer thicknesses, the growth of Ga:Ge is pseudomorphic (commensurate) with the underlying Ge matrix; the atomic planes on both sides of each interface are in perfect registry with each other. This demonstration of fine thickness control, commensurate interfaces, and homogeneous dopant distribution exhibits all of the necessary structural requirements for the fabrication of low-disorder superconducting devices that have been proposed to mitigate loss channels in quantum information applications [24].

Evaluating the phonon spectra of the pure Ge and hyperdoped Ge films using Raman backscattering spectroscopy (Figure 3g), the high p-type concentration produces a new mode near 280 cm^{-1} , which is assigned to a LO phonon hole-plasmon coupled mode (LOPC) [32]. A consequence of the LOPC mode is the screening of the Ge-Ge LO mode, which is now coupled to the large hole concentration and explains its significant reduction in the doped specimen. Comparing the Raman spectra in Figure 3g, both doped and undoped samples yield comparable Raman signals related to the Si-Si and Si-Ge-type sublattices. For the Si-Si LO vibration originating from the thin Si layers, the low dimensionality and diffusion of Ge and Ga atoms into this region lead to a significant mode softening and a strong Si-Ge band near 400 cm^{-1} (Figure 3c) [33]. As both doped and control films exhibit similar Si-Si, Si-Ge, and Ge-Ge bands, and only differ by

the LOPC, we infer high Ga doping does not appreciably affect the growth process.

C. Observation of crystalline distortion

We next resolve the microstructure of the hyperdoped heterostructure using a combination of synchrotron-based grazing incidence X-ray scattering experiments. The 2D grazing-incidence small-angle x-ray scattering (GISAXS) pattern presented in Figure 4a was recorded at the critical angle of the Ga:Ge layers (0.26°), which is well above the critical angle of the relatively less dense Si layers (Figure S11). Pronounced Keising fringes directed in the out-of-plane direction emerge due to the interference of scattered photons within the Ga:Ge epitaxial film and are evidence of relatively sharp interfaces between the different layers. We employed X-ray reflectometry (XRR) to derive the electron density profile and compositional grading parameters (rms roughness) of the film in the normal direction. Based on the XRR fit shown in Figure 4b, compositional grading is confirmed between the layers and diffusion is revealed to be asymmetrical with respect to the stack, with larger roughness values determined for Si grown on top of Ga:Ge, compared to Ga:Ge grown on the Si layer.

The quasi-homoepitaxial growth of the hyperdoped film forces in-plane lattice matching to the substrate, but the larger radius of Ga atoms leads to a predicted out-of-plane tetragonal distortion with the lattice parameter expanding by $\sim 0.12\%$ relative to pure Ge. To experimentally probe this distortion in our system, we employed grazing-incidence wide-angle x-ray scattering (GIWAXS) recorded at the critical angle of Ga:Ge (Figure S12) to maximize scattering intensity within the hyperdoped layer and take advantage of waveguide-like effects[35]; Figure 4d. Due to the similar densities of the Ge substrate ($5.32 \text{ g}\cdot\text{cm}^{-3}$) and the Ga:Ge layer ($5.17 \text{ g}\cdot\text{cm}^{-3}$), a background signal emerges from the (001)-oriented Ge substrate and is outlined by the dotted lines in the 2D GIWAXS image. Notably, these are only resolved on a log scale and constitute the smoothly changing background of the integrated 1D scattering profile shown in Figure 4e. However, near the critical grazing angle, we observe intense Bragg peaks emerging from the hyperdoped layer, with their indexed peaks highlighted in Figure 4d. As predicted, the symmetry of the hyperdoped layer is reduced due to epitaxial clamping and biaxial stress, as evidenced by the splitting of the $\{220\}$ family of Bragg peaks in Figure 4e, and an asymmetry in the $\{311\}$ peak. Due to the substrate clamping effect, the hyperdoped Ge film adopts a body-centered tetragonal unit cell, similar to the archetypal β -Sn (tetragonal space group I41/amd). Assuming the elastic constants of the hyperdoped layer ($\sim 11.22\%$ Ga substitution) are comparable to pure Ge [36], the in-plane lattice mismatch is accommodated by elastic strain and a biaxial stress of $\sigma = 106 \text{ MPa}$ (see Methods section for details of the calculations).

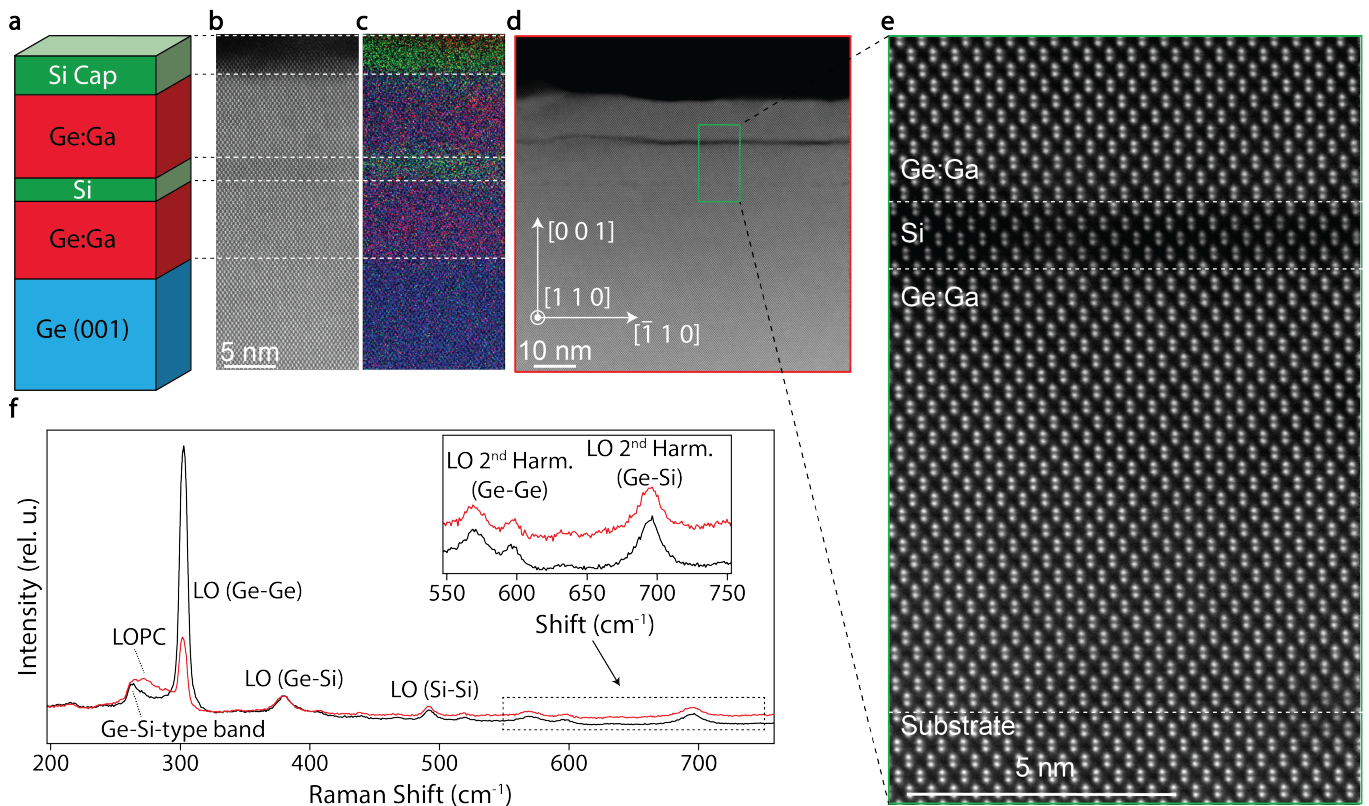


FIG. 3. **a**, Schematic of the film structure as grown by MBE. **b-c**, Cross-sectional TEM/EDS imaging of the TC = 3.5 K hyperdoped sample presenting the compositional profile across the entire film thickness. **d**, Low-magnification cross-sectional HAADF-STEM image of the film. **e**, Zoom-in on the film/substrate and Ga:Ge/Si interfaces, displaying coherent crystalline interfaces. **f**, Raman back-scattering spectra of undoped (black) and doped (red) structures using 532 nm laser excitation at room temperature. The inset highlights the common emergence of highly anharmonic second-order optical bands.

III. CONCLUSIONS

In conclusion, our results establish that MBE growth of hyperdoped Ga:Ge exhibits superconductivity arising from substitutional Ga incorporation, allowing for the creation of coherent semiconductor-superconductor interfaces. TEM and EDS imaging confirm pristine structural and compositional homogeneity. Synchrotron-based methods confirm Ga occupies substitutional sites within the Ge lattice and the interplay between Ga incorporation and epitaxial constraints (substrate clamping) leads to a subtle tetragonal (β -Sn) distortion which aligns with our DFT structural model. Electronic structure calculations show that Ga incorporation at substitutional sites shifts the Fermi level into the valence band and flattens electronic bands at the R point, likely promoting superconductivity. Our findings highlight the intrinsic nature of superconductivity in hyperdoped Ga:Ge and underscore its potential as a scalable platform for epitaxial semiconductor-superconductor heterostructures using the mature group IV semiconductor toolkit.

IV. SUPPLEMENTARY INFORMATION

A. Methods

Thin film growth: The materials used in this study are all grown in a custom Varian Gen II molecular beam epitaxy (MBE) system on 50.8 mm undoped Ge (001) wafers. Prior to loading into vacuum, the wafers are etched in deionized water at 90°C for 15 minutes and then immediately loaded into the vacuum chamber on indium-free mounting blocks. The wafers are sequentially outgassed inside the growth reactor at 250°C, 450°C, and finally 650°C, for 15 minutes, 15 minutes, and 5 minutes, respectively, then cooled to room temperature for growth. Pure germanium (6N) and silicon (3N) source material is deposited via Thermionics HM2 e-Guns operating at a 6 kV acceleration voltage. Gallium doping is done with a standard Knudsen effusion cell source (MBE Komponenten). Atomic fluxes are measured prior to growth with a retractable quartz crystal microbalance placed in the center of the growth path in front of the substrate. The substrate is faced away from the atomic beam path(s) during flux measurement. Reported temperatures are from a thermocouple attached close to the

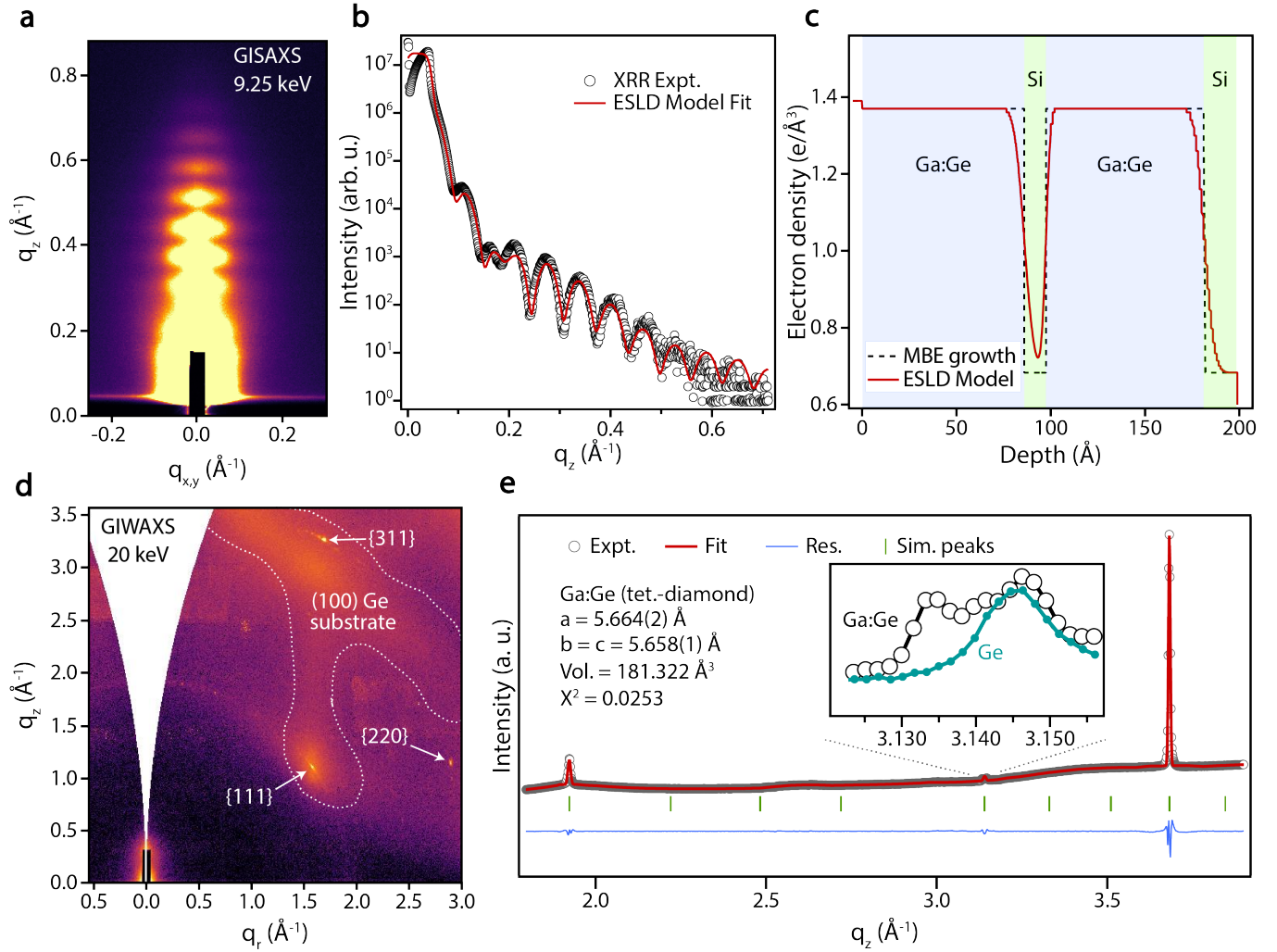


FIG. 4. **a**, 2D GISAXS pattern of the Ga:Ge epitaxial film recorded at the critical angle (0.26°) of the superconducting layer. The intensity map is on a linear scale. **b**, The out-of-plane X-ray reflectivity measurement of the Ga:Ge film with a fit made using the REFLEX software package [34]. **c**, Cross-section of the electron scattering length density (ESLD) of the epitaxial stack derived for the fitting model of the fringes in **b**. **d**, 2D GIWAXS pattern of the Ga:Ge thin film record at the critical angle (0.125°). The color map is on a log scale. The family of crystallographic planes giving rise to the intense Bragg reflections of the hyperdoped layer are identified with arrows. **e**, Corresponding integrated GIWAXS profile (q_{xyz}) and its subsequent structural refinement (Le Bail method). The refined unit cell parameters are displayed and an expansion of the split 220 family of Bragg peaks is inset to highlight the reduced symmetry of the clamped Ga:Ge epitaxial layer in comparison to the undoped Ge control.

backside of the substrate that has been calibrated to the GaAs (001) oxide-removal temperature. Samples are grown with a Ge flux of $\sim 8-8.5 \times 10^{13}/\text{cm}^2\text{s}$, a Ga flux of $1.4-1.9 \times 10^{13}/\text{cm}^2\text{s}$, and a Si flux of $2.5-3 \times 10^{13}/\text{cm}^2\text{s}$. The nominally 20 nm thick films are grown as follows, as described in Ref. [30]: (1) 10 nm of Ga-doped Ge, (2) 0.5 nm of Si, (3) 10 nm of Ga-doped Ge, (4) 1 nm Si cap. Film growth is monitored using reflection high-energy electron diffraction (RHEED) along a $\langle 110 \rangle$ cut (beam path \parallel to $\langle 010 \rangle$). Representative RHEED images throughout the growth steps are presented in Figure S5.

Four-point transport measurements: Electrical characterization is done in an Oxford TeslatronPT He4

cryostat using a HelioxVT He3 probe insert with a base temperature of ~ 270 mK and magnetic field capabilities up to 12 T. Measurements are collected using a standard Van der Pauw wiring configuration on square pieces cleaved from near the center of each wafer. On-chip contacts are made via annealed In-Sn eutectic alloy at each of the four corners which are then wired to a daughter-board using gold wire.

First-principles calculations: First-principles calculations were performed using DFT as implemented in VASP [37, 38]. Projector augmented wave (PAW) pseudopotentials including semicore 3d electrons were adopted, with a plane-wave cutoff of 550 eV. A $7 \times 7 \times 7$

Γ -centered k-point mesh was used to sample the Brillouin zone of the conventional 8-atom unit cell of Ge (cubic diamond structure, space group $Fd\bar{3}m$). Structural optimizations were performed using the PBEsol exchange-correlation functional [39], which yields lattice parameters in excellent agreement with the experiment (see Table S1), and a convergence threshold of 0.005 eV/Å on all forces.

For the Ga-doped Ge structure with substitutional fine-structure, one host atom in the 8-atom unit cell is replaced by a Ga atom, corresponding to a doping concentration of 12.5%. Conversely, interstitial doping is modeled by placing one Ga atom at interstitial doping sites, representing a doping concentration of 11.1%. To model the effect of substrate clamping in Ga-doped Ge, the in-plane lattice parameters were fixed to the pristine Ge values, and only the out-of-plane lattice parameter was allowed to relax. K-edge spectra were simulated using the supercell core-hole method [40] within a $2 \times 2 \times 2$ supercell containing 64 atoms (72 atoms in the case of interstitial doping). The formation energy of a neutral Ga dopant in the Ge crystal is calculated as $E_{Form} = E_d - E_p - \sum_i n_i \mu_i$, where E_d is the total energy of the structure containing the defect, E_p is the total energy of the pristine structure, n_i is the number of atoms of species i being added ($n > 0$) or removed ($n < 0$), and μ_i is the chemical potential. For Ga, this is the energy per atom of a Ga crystal (base-centered orthorhombic structure).

To calculate the electronic band structure and density of states, we adopted the MBJLDA meta-GGA functional [41] based on the modified Becke-Johnson exchange functional. This functional has been shown to yield excellent results for the band structure and band gap of many semiconductors, including Ge [42, 43], which standard semilocal DFT predicts erroneously to be metallic. Spin-orbit coupling was included in all electronic structure calculations. A denser $20 \times 20 \times 20$ k-mesh was employed to compute the density of states. To accurately determine the Fermi-level shifts in Ga-doped Ge, a $31 \times 31 \times 31$ k-mesh was used.

Scanning transmission electron microscopy:

Cross-sectional specimens for scanning transmission electron microscopy (S/TEM) analysis were prepared using a focused ion beam (FIB) system (FEI Helios NanoLab 600 DualBeam). To minimize surface damage, the samples were thinned and polished with Ga ions at 5 kV. S/TEM imaging and energy-dispersive X-ray spectroscopy (EDS) were conducted using a Thermo Fisher Scientific Themis-Z microscope. The instrument operated at an accelerating voltage of 300 kV with a semi-convergence angle of 20 mrad. HAADF-STEM images were collected using a 64–200 mrad high-angle annular dark field (HAADF) detector. High-resolution images were acquired through multiple rapid scans (2048×2048 pixels, 200 ns per pixel), which were combined to improve the signal-to-

noise ratio. EDS analysis was performed with the Super-X EDS detector, and the elemental mappings are presented as net count images.

Raman Spectroscopy: Raman spectra were recorded from the thin film surface in a backscattering configuration, using an integrated Edinburgh confocal microRaman instrument (RM5). Excitation was provided by one of three solid-state laser lines (532 nm, 638 nm and 785 nm) and focused on the surface using a long working lens (Olympus, 10 \times , 0.4 NA). Dispersion was achieved through a 1200 g/mm diffraction grating (spectral resolution 0.2 cm^{-1}), instrument calibration was verified through checking the position of the Si band at $\pm 520.7 cm^{-1}$, and spectra were recorded using a thermoelectric CCD detector. Changes to the local vibrational structure of the hyperdoped film are first confirmed through the evaluation of the excitation energy dependence of the Raman back-scattering signals (Figure S7). At longer excitation wavelengths (785 nm), both the control and target films exhibit comparable Raman response, while more surface-sensitive information is recovered at shorter wavelengths (532 nm) to resolve differences in the thin films (Figure 3f).

Synchrotron-based GISAXS/GIWAXS: To identify the crystalline phases and microstructure of films, synchrotron-based grazing incidence wide-angle X-ray scattering (GIWAXS) data were collected at the small angle X-ray scattering/wide angle X-ray scattering (SAXS/WAXS) beamline at the Australian Synchrotron [44]: 2D scattering patterns were recorded using a wavelength of either 1.340375 Å (9.25 keV) or 0.619924 Å (20 keV), using an energy-selective Pilatus 2M detector. The measurements made using a 20 keV beam energy were to increase the observed Q-range for the structural refinements, using an energy threshold of 15 keV to suppress the X-ray fluorescence signals arising from the excited K-edges of Ge (11.1 keV) and Ga (10.37 keV). Experiments at 9.25 keV had no such issues. Two different sample-to-detector distances were employed to record both SAXS (5.5 m) and WAXS (0.45 m) profiles, each calibrated using a silver behenate reference standard. The sample and detector were enclosed in a vacuum chamber to suppress air scatter. Scattering patterns were measured as a function of the angle of incidence, with data shown acquired with an angle of incidence near the critical angle (for a given X-ray energy) to maximize scattering intensity from the sample. All collected 2D images were azimuthally integrated using PyFAI [45] and processed using a custom Python routine. The resulting unit cell models were refined using the La Bail method implemented in Fullprof[46], a comprehensive analysis software. In line with our other characterization techniques, our GIWAXS experiments failed to detect Ga droplet formation or segregation within the film. Due to the relatively small scattering volume of the Si layers, no additional peaks are indexed to this phase either.

Stress analysis: The lattice mismatch is accommodated by an elastic strain in the hyperdoped epilayer, giv-

ing a biaxial stress of $\sigma = 2\mu f \cdot (1 + \nu)/(1 - \nu)$, where μ is the shear modulus, ν Poisson's ratio and f the misfit parameter. Assuming the hyperdoped Ga:Ge epilayer forms a cubic unit cell when unconstrained, elastic isotropy is assumed in the relevant deformation directions and the misfit parameter is given by $f = (a_{Ga:Ge} - a_{Ge})/a_{Ge}$, where $a_{Ga:Ge}$ and a_{Ge} are the lattice parameters of the relaxed epilayer and substrate, respectively. We do not have such experimental data for the relaxed hyperdoped unit cell, however, since the epilayers studied here are pseudomorphically grown (Figure 3e), the values obtained from the structural refinement can be related to the relaxed lattice parameter of the Ga:Ge layer through $a_{Ga:Ge} = a_{Ge}[1 + P(\Delta d/d)_{\perp}]$, where P is the elastic parameter of the films [47]. Regardless of the growth direction, the in-plane and out-of-plane biaxial strain components are given by $\epsilon_{\parallel} = (a_{Ga:Ge} - a_{Ge})/a_{Ge}$ and $\epsilon_{\perp} = \epsilon_{\parallel}(1 - 1/P)$, respectively. For our thin films grown on Ge (100); $P_{100} = C_{11}/(C_{11} + 2C_{12}) = 0.5709$. To implement our calculation, we approximate the elastic constants C_{ij} of the hyperdoped film to be comparable to the pure Ge crystal [47] (as there is no relevant data for GaGe alloys). Based on our hole carrier concentrations, the Ga concentration for the sample studied in Figure 3e is $\sim 11.22\%$ and has a calculated relaxed (cubic) lattice parameter of $a_{Ga:Ge} = 5.6614 \text{ \AA}$, which is 0.11% larger than the Ge crystal.

Synchrotron-based EXAFS experiments: Ga K-edge X-ray absorption spectra (XAS) were captured at the Australian Synchrotron (ANSTO in Clayton, Victoria) MEX1 beamline. A double-crystal Si (111) monochromator equipped with focusing optics was used to reduce harmonic content while producing excitation energy. An inline Ga₂O₃ reference (the initial peak of the first derivative occurs at 10.3687 keV) was used to calibrate the monochromator at Ga-K absorption edge with E0 set to its known value of 10.3671 eV. All acquisitions were performed on thin film materials in a fluorescent mode. Brief XAS scans of specific samples were conducted to verify the stability of the materials under at least several minutes of X-ray exposure before the full acquisitions. Samples were measured with varying energy intervals over the pre-edge (5 eV) and the XANES region (0.25), with 0.035 intervals in k-space over the EXAFS. At low-k an integration time of 1 s was employed per interval, with longer integration times weighted toward high-k portions of the spectrum, up to a maximum value of 9 in k-space (max of 2 s). Multiple scans were collected at different positions of the sample. Data processing including background subtraction, scan averaging, edge-height normalization, and rebinning was performed based on the Athena program[48]. For normalization of energy spectra and removal of background, the pre-edge range was set between -150 eV and -30 eV, while the normalization range spanned from 80 to 300 eV post-edge. The order of normalization was designated as 3. For the presented EXAFS data, the k-weight was configured as 2, and the k-range for the forward Fourier transform was

defined from 0.8 to 8.5.

EXAFS fine-structure modeling: Fits was conducted in the ARTEMIS, part of the IFEFFIT software package[48]. The scattering paths used to evaluate and model the data were derived from the optimized crystal structures with different defects. Using these input structures to derive the scattering paths, the only agreeable fine structure accounting for the dominant EXAFS signal arising from an R fitting window of 1.8 to 5.1 \AA emerged using the calculated Ga substituted structure. To simulate the Ga substituted Ge crystal fine structure, the input paths out to 5 \AA are determined using the DFT-derived Ga substitutionally doped Ge structure and the FEFF package[48], with a distance fuzz = 0.030 \AA . This generated 6 unique scattering pairs centered on the Ga substitutional site, with some other lower ranked paths omitted from the actual model to avoid over-fitting (see Table S2). A common scaling factor has been used on all path distance corrections to account for the difference between the DFT simulated unit cell volume and the experiment crystal volume at room temperature. A phase correction has been made to Figure 2d in the main text using the most intense Ga-Ge single scattering path, near 2.45 \AA . The data were ultimately fit using 18 variables and 26 independent points, resulting in a reasonable R-factor of 0.015. The fitting was conducted in R-space using multiple k-weightings, with $k = 1, 2$ and 3 . Errors of individual fit parameters were determined using ARTEMIS to take into account the correlations between parameters and known parameters without error estimates were fixed during the fit.

X-ray Reflectometry: The X-ray reflectometry patterns of the thin film samples were collected using a Rigaku SmartLab X-ray diffractometer with a goniometer radius of 300 mm, under CuK α radiation ($\lambda = 1.54059 \text{ \AA}$, 40kV 40mA). The X-ray was converged into a parallel beam using a parabolic multi-layer mirror in a CBO-PB module, followed by a channel-cut Ge 2x(220) monochromator. A fixed incident slit of 0.1 mm was used for fine angular resolution. The thin films were precisely aligned according to its specular reflection on top of a RxRy double tilt attachment on a ϕ rotation stage. A 0.2 mm anti-scattering slit and a 0.3 mm detector slit were used to enhanced the signal intensity. Both the primary and secondary sides use a 5° soller slit to control axial divergence. Each pattern was collected by a Hypix3000 detector in 0D mode from 0 to $10^\circ 2\theta$ with a 0.01° step size and at a speed of $0.1^\circ 2\theta \cdot \text{min}^{-1}$. Fits to patterns were made using the REFLECT standalone reflectivity fitting software[34].

B. Supporting Data

Structure	Lattice Parameter (\AA^3) $\mathbf{a}=\mathbf{b}, \mathbf{c}$	Volume (\AA^3)	Crystal Structure	E_{Form} (eV)
Pure Ge	5.674, 5.674	182.64	Cubic	
Sub. Ga:Ge	5.674, 5.681	182.87	Tetragonal	0.314
Int. Ga:Ge	5.674, 6.220	200.128	Tetragonal	1.946

TABLE S1. Structural parameters of DFT optimized structures for pure and Ga-doped Ge (substitutional and interstitial doping) and calculated defect formation energies E_{Form} .

Path type	Degen.	Rank	$\mathbf{R}(\text{\AA})$	$\sigma^3 (\text{\AA}^2)$	ΔE_0 (eV)	$\mathbf{S0}_2$	R-factor
Ga-Ge (SS)	4	100	2.451(1)	0.0051(4)			
Ga-Ge (SS)	12	90.82	4.002(5)	0.0063(2)			
<i>Ga-Ge-Ge (DS)</i>	<i>12</i>	<i>5.71</i>	<i>4.450</i>				
Ga-Ge-Ge (DS)	24	21.4	4.452(2)	0.010(6)	-0.195	0.68(11)	0.015
Ga-Ge (SS)	12	59.45	4.693(2)	0.0087(5)			
<i>Ga-Ge-Ge (R)</i>	<i>4</i>	<i>4.09</i>	<i>4.900</i>				

TABLE S2. EXAFS fitting parameters extracted from fits made to spectra recorded at 295 K using a Ga substitutional model. The lower ranked paths (in italics) are omitted from the actual fit model to avoid overfitting. The errors provided in the parentheses align with the last significant figures of the variable fit values. Further fitting details can be found in the Methods section. The path type can be tracked as: SS – single scattering pair; DS – double scattering; R – rattle.

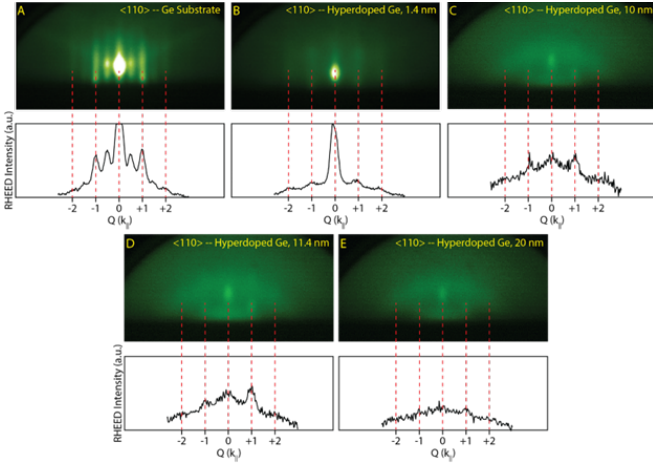


FIG. S5. RHEED line cuts for superconducting hyperdoped Ge thin film. **a**, Ge substrate $\langle 110 \rangle$ -type direction, taken at room temperature just before deposition of Ga:Ge film. **b**, Initial surface of Ga:Ge film. **c**, RHEED pattern after the first 10 nm of Ga:Ge deposited. **d**, After the Si spacer layer and initial growth of the second Ga:Ge layer. **e**, End of Ga:Ge growth, before Si cap is deposited. We note a superimposed amorphous ring over a faint $\langle 110 \rangle$ -type direction diffraction pattern. This is consistent with previous observations that Ga-adsorption at low temperatures creates a floating layer at the surface from which the incorporated dopants are taken[49].

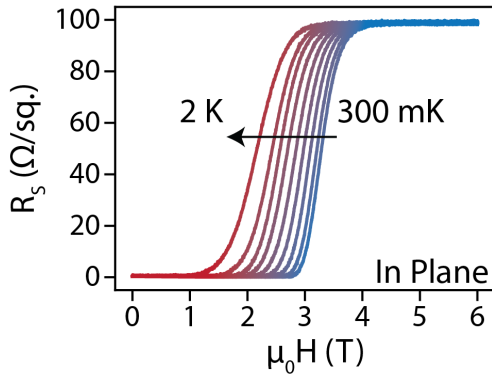


FIG. S6. In-plane critical magnetic field behavior for the sample presented in Figure 1b-c.

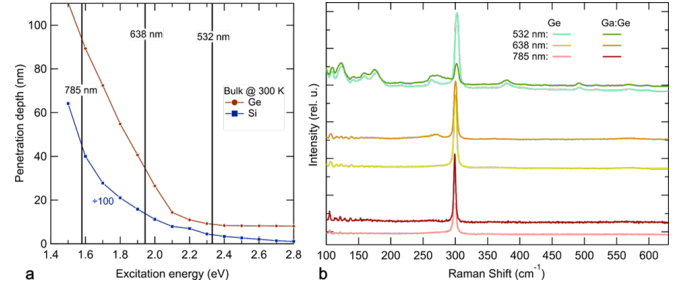


FIG. S7. **a**, Raman Scattering penetration depth (d_{RS}) as a function of the laser excitation energy, determined by considering the absorption coefficients[50] for both the incoming (α_{out}) and the outgoing (α_{in}) light: $d_{RS} = 1/(\alpha_{in} + \alpha_{out}) \approx 1/\alpha_{in}$. **b**, Comparison of Raman spectra recorded from Ga:Ge and Ge control MBE films at different excitation energies. At longer excitation wavelengths (785 nm), both the control and target films exhibit a comparable Raman response. Probing the surface-sensitive information with shorter wavelengths, the differences between the vibrational structure of the films become clearer. The appearance of disorder-activated LA modes below 200 cm^{-1} (from both Ge-type and Si-type sublattices) in the scattering volume yields comparable scattering intensities under these conditions for the control and doped sample. We suggest the origins of these bands are a combination of (local) lattice strain, phonon confinement and (partial) satisfaction of the resonance conditions of the Ge crystal $E_1 + \Delta_1$ gap[51]. Together, these features break the normal Raman scattering selection rules of a normal (001)-oriented bulk Ge film, i.e., resembling more the Raman spectra recorded using 785 nm laser light.

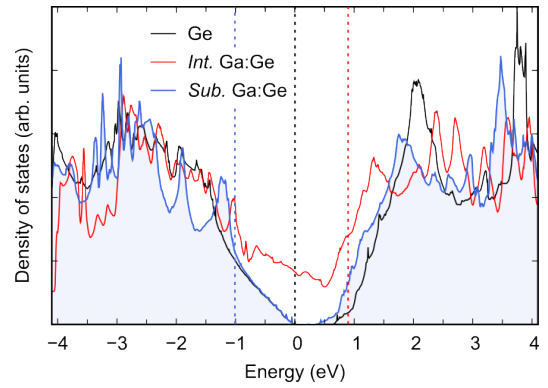


FIG. S8. Total and projected density of states of the hyperdoped Ga:Ge crystal shown in Figure 2a of the main text with substitutional fine-structure.

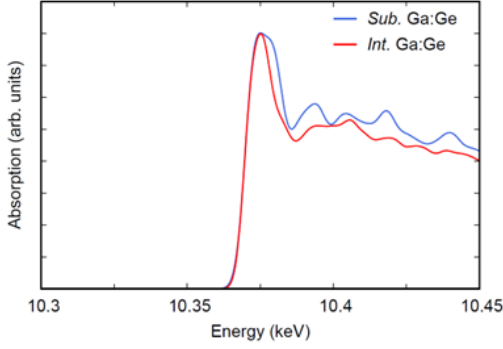


FIG. S9. Simulated X-ray absorption spectra of Ga K-edge for Ga:Ge crystals with substitutional and interstitial doping sites.

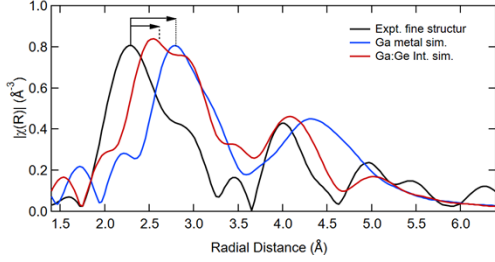


FIG. S10. Comparison of the simulated fine structure derived from the CIF files of Ga:Ge interstitial system (DFT calculated system in Figure 2a of main text) and amorphous Ga metal[31]. Note that these Fourier transforms have been phase corrected, for simplicity. The arrows highlight the relatively large difference in experimental bond length of the nearest-neighbor scattering pair and those derived in the simulations.

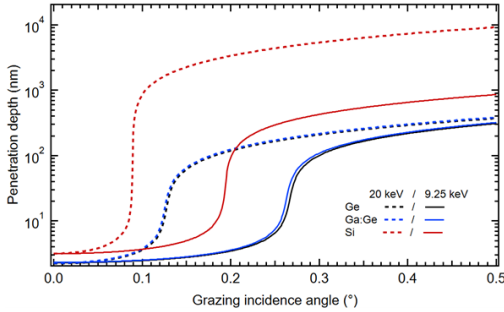


FIG. S11. The calculated penetration depth of the different material layers at the synchrotron energies used for grazing incidence experiments. For the range of angles below and at the critical angle, the X-ray electromagnetic field only interacts a short distance below the film surface due to the evanescent damping (5 - 10 nm), and constitutes the defined evanescent regime.

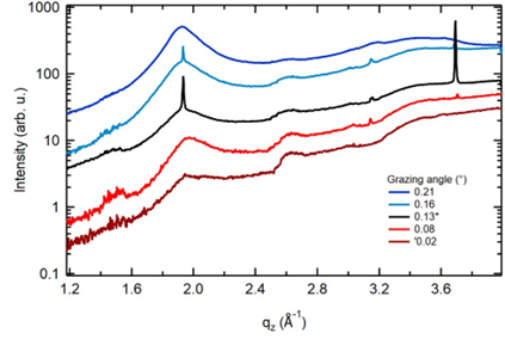


FIG. S12. Evolution of the integrated GIWAXS signal recorded from the Ga:Ge film as a function of the grazing incidence angle (α_i : values inset). Here * identifies the calculated critical angle for the doped Ga:Ge layer at an X-ray beam energy of 20 keV. As the angle of incidence nears the critical angle of the doped layer, the Bragg reflections emerging begin to intensify. A combination of lateral steps ($200 \mu\text{m}$) made between each incident angle frame, mechanical jolting, and imperfect beam divergence means the critical angle conditions (waveguide type effect) is relatively really sensitive and results in the discontinuity of some profile features between frames.

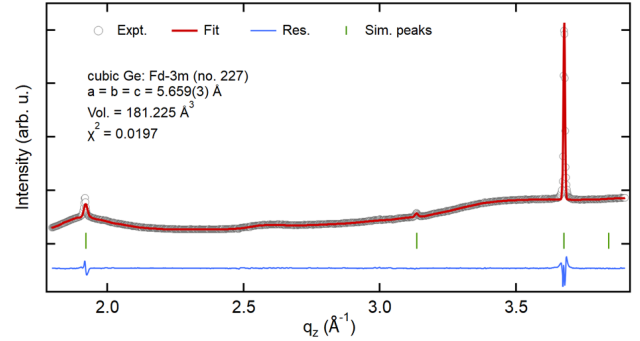


FIG. S13. Integrated GIWAXS profile (q_{xyz}) and structural refinement (Le Bail method) of the pure Ge epitaxial layer. Unstrained Ge crystal belongs to the high-symmetry cubic space group $Fd\bar{3}m$ (space group No. 227), characterized by equivalent lattice parameters ($a=b=c$) and a structural refinement of our undoped Si-Ge film aligns well with the reported bulk, cubic value ($a = 5.657906(9) \text{ \AA}$, Vol. = 181.1203 \AA^3)[52]

ACKNOWLEDGMENTS

NYU team acknowledges funding support from the United States Air Force Office of Scientific Research award number FA9550-21-1-0338. We acknowledge computational resources at the NCI National Facility through the National Computational Merit Allocation Scheme. J.A.S. acknowledges financial support from the Australian Research Council (DE230100173); Y-H.C. and P.J. acknowledge support from the Australian Research Council (LP210200636, CE170100009); C.V. acknowledges financial support from the Australian Research Council (DE220101147). This research was under-

taken on the X-ray Absorption Spectroscopy and the SAXS/WAXS beamlines at the Australian Synchrotron, part of ANSTO. The XRR data reported in this paper were obtained at the Central Analytical Research Facility operated by Research Infrastructure (QUT). Electron microscopy was performed at the Center for Electron Microscopy and Analysis (CEMAS) at The Ohio State University. S.S.-R. acknowledges Dan Huber for assisting with TEM sample preparation.

References

-
- [1] J. Shabani, M. Kjaergaard, H. J. Suominen, Y. Kim, F. Nichele, K. Pakrouski, T. Stankevic, R. M. Lutchyn, P. Krogstrup, R. Feidenhans'l, S. Kraemer, C. Nayak, M. Troyer, C. M. Marcus, and C. J. Palmstrøm, *Phys. Rev. B* **93**, 155402 (2016).
- [2] R. M. Lutchyn, E. P. A. M. Bakkers, L. P. Kouwenhoven, P. Krogstrup, C. M. Marcus, and Y. Oreg, *Nat. Rev. Mater.* **3**, 52 (2018).
- [3] V. Mourik, S. M. Frolov, S. R. Plissard, E. P. A. M. Bakkers, and L. P. Kouwenhoven, *Science* **336**, 1003 (2012).
- [4] L. Casparis, T. W. Larsen, M. S. Olsen, F. Kueemmeth, P. Krogstrup, J. Nygård, K. D. Petersson, and C. M. Marcus, *Phys. Rev. Lett.* **116**, 150505 (2016).
- [5] L. Casparis, M. R. Connolly, M. Kjaergaard, N. J. Pearson, A. Kringhøj, T. W. Larsen, F. Kueemmeth, T. Wang, C. Thomas, S. Gronin, G. C. Gardner, M. J. Manfra, C. M. Marcus, and K. D. Petersson, *Nat. Nanotechnol.* **13**, 915–919 (2018).
- [6] W. M. Strickland, L. J. Baker, J. Lee, K. Dindial, B. Heiba Elfeky, P. J. Strohhoben, M. Hatefipour, P. Yu, I. Levy, J. Issokson, V. E. Manucharyan, and J. Shabani, *Phys. Rev. Research* **6**, 023094 (2024).
- [7] W. M. Strickland, B. Heiba Elfeky, L. J. Baker, A. Mairani, J. Lee, I. Levy, J. Issokson, A. Vrajitoarea, and J. Shabani, *arXiv:2406.09002* (2024).
- [8] A. Danilenko, D. Sabonis, G. W. Winkler, O. Erlandsson, P. Krogstrup, and C. M. Marcus, *Phys. Rev. B* **108**, L020505 (2023).
- [9] M. Lodari, O. Kong, M. Rendell, A. Tosato, A. Sammak, M. Veldhorst, A. R. Hamilton, and G. Scappucci, *Appl. Phys. Lett.* **120**, 122104 (2022).
- [10] G. Scappucci, C. Kloeffer, F. A. Zwanenburg, D. Loss, M. Myronov, J.-J. Zhang, S. De Franceschi, G. Katsaros, and M. Veldhorst, *Nat. Rev. Mater.* **6**, 926 (2021).
- [11] A. Sammak, D. Sabbagh, N. W. Hendrickx, M. Lodari, B. Paquelet Wuetz, A. Tosato, L. Yeoh, M. Bollani, M. Virgilio, M. A. Schubert, P. Zaumseil, G. Capellini, M. Veldhorst, and G. Scappucci, *Adv. Func. Mater.* **29**, 1807613 (2019).
- [12] A. Tosato, V. Levajac, J.-Y. Wang, C. J. Boor, F. Borsoi, M. Botifoll, C. N. Borja, S. Martí-Sánchez, J. Arbiol, A. Sammak, M. Veldhorst, and G. Scappucci, *Commun. Mater.* **4**, 23 (2023).
- [13] W. F. Schiela, P. Yu, and J. Shabani, *PRX Quantum* **5**, 030102 (2024).
- [14] S. Das Sarma and H. Pan, *Phys. Rev. B* **103**, 195158 (2021).
- [15] P. Krogstrup, N. L. B. Ziino, W. Chang, S. M. Albrecht, M. H. Madsen, E. Johnson, J. Nygård, C. M. Marcus, and T. S. Jespersen, *Nat. Mater.* **14**, 400 (2015).
- [16] T. D. Sands, C. J. Palmstrøm, J. P. Harbison, V. G. Keramidas, N. Tabatabaie, T. L. Cheeks, R. Ramesh, and Y. Silberberg, *Mater. Sci. Rep.* **5**, 99 (1990).
- [17] P. J. Strohhoben, S. Manzo, V. Saraswat, K. Su, M. S. Arnold, and J. K. Kawasaki, *ACS Appl. Mater. Interfaces* **13**, 42146 (2021).
- [18] R. Zhao, S. Park, T. Zhao, M. Bal, C. R. H. McRae, J. Long, and D. P. Pappas, *Phys. Rev. Applied* **14**, 064006 (2020).
- [19] B. Heiba Elfeky, W. M. Strickland, J. Lee, J. T. Farmer, S. Shanto, A. Zarassi, D. Langone, M. G. Vavilov, E. M. Levenson-Falk, and J. Shabani, *PRX Quantum* **4**, 030339 (2023).
- [20] A. E. Svetogorov, D. Loss, and J. Klinovaja, *Phys. Rev. B* **105**, 174519 (2022).
- [21] D. Frombach and P. Recher, *Phys. Rev. B* **101**, 115304 (2020).
- [22] C. Müller, J. H. Cole, and J. Lisenfeld, *Rep. Prog. Phys.* **82**, 124501 (2019).
- [23] S. Das Sarma, M. Freedman, and C. Nayak, *Npj Quantum Inf.* **1**, 15001 (2015).
- [24] Y.-P. Shim and C. Tahan, *Nat. Commun.* **5**, 4225 (2014).
- [25] E. A. Ekimov, V. A. Sidorov, E. D. Bauer, N. N. Mel'nik, N. J. Curro, J. D. Thompson, and S. M. Stishov, *Nature* **428**, 542 (2004).
- [26] T. Hermannsdörfer, V. Heera, O. Ignatchik, M. Uhlarz, A. Mücklich, M. Posselt, H. Reuther, B. Schmidt, K.-H. Heinig, W. Skorupa, M. Voelskow, C. Wündisch, R. Skrotzki, M. Helm, and J. Wosnitza, *Phys. Rev. Lett.* **102**, 217003 (2009).
- [27] S. Prucnal, V. Heera, R. Hübner, M. Wang, G. P. Mazur, M. J. Grzybowski, X. Qin, Y. Yuan, M. Voelskow, W. Skorupa, L. Rebohle, M. Helm, M. Sawicki, and S. Zhou, *Phys. Rev. Mater.* **3**, 054802 (2019).
- [28] K. Sardashti, T. D. Nguyen, W. L. Sarney, A. C. Leff, M. Hatefipour, M. C. Dartiaill, J. Yuan, W. Mayer, and J. Shabani, *Phys. Rev. Mater.* **5**, 064802 (2021).
- [29] F. A. Trumbore, *Bell Syst. Tech. J.* **39**, 205 (1960).
- [30] P. J. Strohhoben, A. M. Brook, W. L. Sarney, and J. Sha-

- bani, *AIP Adv.* **13**, 085118 (2023).
- [31] B. D. Sharma and J. Donohue, *Z. Kristallogr. Cryst. Mater.* **117**, 1 (1962).
- [32] A. Compaan, G. Contreras, M. Cardona, and A. Axmann, *MRS Proc.* **23**, 117 (1983).
- [33] J.-H. Fournier-Lupien, S. Mukherjee, S. Wirths, E. Pippe, N. Hayazawa, G. Mussler, J. M. Hartmann, P. Desjardins, D. Buca, and O. Moutanabbir, *Appl. Phys. Lett.* **103**, 263103 (2013).
- [34] G. Vignaud and A. Gibaud, *J. Appl. Crystallogr.* **52**, 201 (2019).
- [35] J. A. Steele, E. Solano, D. Hardy, D. Dayton, D. Ladd, K. White, P. Chen, J. Hou, H. Huang, R. A. Saha, L. Wang, F. Gao, J. Hofkens, M. B. J. Roeffaers, D. Chernyshov, and M. F. Toney, *Adv. Energy Mater.* **13**, 2300760 (2023).
- [36] H. J. McSkimin and P. Andreatch, *J. Appl. Phys.* **34**, 651.
- [37] G. Kresse and J. Hafner, *Phys. Rev. B* **47**, 558(R) (1993).
- [38] G. Kresse and J. Furthmüller, *Phys. Rev. B* **54**, 11169 (1996).
- [39] J. P. Perdew, A. Ruzsinszky, G. I. Csonka, O. A. Vydrov, G. E. Scuseria, L. A. Constantin, X. Zhou, and K. Burke, *Phys. Rev. Lett.* **100**, 136406 (2008).
- [40] F. Karsai, M. Humer, E. Flage-Larsen, P. Blaha, and G. Kresse, *Phys. Rev. B* **98**, 235205 (2018).
- [41] F. Tran and P. Blaha, *Phys. Rev. Lett.* **102**, 226401 (2009).
- [42] C. Rödl, J. Furthmüller, J. Renè Suckert, V. Armuzza, F. Bechstedt, and S. Botti, *Phys. Rev. Materials* **3**, 034602 (2019).
- [43] E. M. T. Fadaly, A. Dijkstra, J. Renè Suckert, D. Ziss, M. A. J. van Tilburg, C. Mao, Y. Ren, V. T. van Lange, K. Korzun, S. Kölling, M. A. Verheijen, D. Busse, C. Rödl, J. Furthmüller, F. Bechstedt, J. Stangl, J. J. Finley, S. Botti, J. E. M. Haverkort, and E. P. A. M. Bakkers, *Nature* **580**, 205 (2020).
- [44] N. M. Kirby, S. T. Mudie, A. M. Hawley, D. J. Cookson, H. D. T. Mertens, N. Cowieson, and V. Samardzic-Boban, *J. Appl. Crystallogr.* **46**, 1670 (2013).
- [45] G. Ashiotis, A. Deschildre, Z. Nawaz, J. P. Wright, D. Karkoulis, F. E. Picca, and J. Kieffer, *J. Appl. Crystallogr.* **48**, 510 (2015).
- [46] J. Rodríguez-Carvajal, *Physica B: Condensed Matter* **192**, 55 (1993).
- [47] H. J. McSkimin and P. Andreatch Jr., *J. Appl. Phys.* **34**, 651 (1963).
- [48] B. Ravel and M. Newville, *J. Synchrotron Rad* **12**, 537 (2005).
- [49] V. Kesan, S. Iyer, and J. Cotte, *Journal of Crystal Growth* **111**, 847 (1991).
- [50] D. E. Aspnes and A. A. Studna, *Physical Review B* **27**, 985 (1983).
- [51] M. I. Alonso and M. Cardona, *Phys. Rev. B* **37**, 10107 (1988).
- [52] J. F. C. Baker and M. Hart, *Acta Cryst.* **A31**, 364 (1975).